



저작자표시-비영리-변경금지 2.0 대한민국

이용자는 아래의 조건을 따르는 경우에 한하여 자유롭게

- 이 저작물을 복제, 배포, 전송, 전시, 공연 및 방송할 수 있습니다.

다음과 같은 조건을 따라야 합니다:



저작자표시. 귀하는 원저작자를 표시하여야 합니다.



비영리. 귀하는 이 저작물을 영리 목적으로 이용할 수 없습니다.



변경금지. 귀하는 이 저작물을 개작, 변형 또는 가공할 수 없습니다.

- 귀하는, 이 저작물의 재이용이나 배포의 경우, 이 저작물에 적용된 이용허락조건을 명확하게 나타내어야 합니다.
- 저작권자로부터 별도의 허가를 받으면 이러한 조건들은 적용되지 않습니다.

저작권법에 따른 이용자의 권리는 위의 내용에 의하여 영향을 받지 않습니다.

이것은 [이용허락규약\(Legal Code\)](#)을 이해하기 쉽게 요약한 것입니다.

[Disclaimer](#)

工學碩士學位論文

**Enhancing the Bass Frequency
Response of PVDF based Thin Film
Acoustic Actuator:
A Relationship between Frequency
Response and Polymer Crystallinity**

저음부가 개선된 PVDF 기반의
박막형 음향 작동기 제조 및
주파수 응답 특성과 결정성과의 관계

2013年 6月

서울대학교 大學院

化學生物工學部

James S. Lee

Abstract

Enhancing the Bass Frequency Response of PVDF based Thin Film Acoustic Actuator: A Relationship between Frequency Response and Polymer Crystallinity

James S. Lee

School of Chemical and Biological Engineering

The Graduate School

Seoul National University

A high-performance polyvinylidene fluoride (PVDF)-based acoustic actuator for bass frequencies was successfully fabricated. High concentrations of Ba-doped SiO₂/TiO₂ hollow nanoparticles (Ba-HNPs) were embedded into PVDF fibers at large-scale *via* electrospinning, enhancing the β -phase content and the dielectric property of the pristine PVDF matrix. A chemical vapor deposition (CVD)-grown graphene

electrode attached to a silane-treated surface of a Ba–HNPs/PVDF thin film enabled high electron mobility and the ability to deliver distortion-free acoustic signals. The frequency response of the synthesized acoustic actuator was studied as a function of the Ba–HNPs content, film thickness, and type of electrode. The optimized thickness of the PVDF-based thin film was *ca.* 80 μm . The outstanding conductivity of the graphene electrode provided enhancement of the frequency response in the middle and treble ranges, respectively. Addition of 15 wt% of Ba–HNPs led to a 60 % increase in frequency response and a 21 % improvement in total harmonic distortion (THD) at bass frequencies. Most of all, it is demonstrated that acoustic performance is strongly effected by degree of crystallinity of PVDF.

Keywords: Acoustic actuator, PVDF, CVD-grown graphene, Hollow nanoparticles, Crystallinity.

Student Number: 2011-24099

Contents

Chapter 1. Introduction	1
1.1 Flexiable Acoustic Acuator	1
1.1.1 Piezoelectric material	1
1.1.2 Nanofiller composite.....	3
1.1.3 Various electrodes	4
1.2 Objective of this study	6
Chapter 2. Experimental.....	8
2.1 Materials	8
2.2 Synthesis of Ba-doped SiO ₂ /TiO ₂	9
2.3 Preparation of the Ba-HNPs/PVDF thin film	10
2.4 Preparation of CVD-grown graphene electrode.....	11
2.5 Fabrication of the Ba-HNPs/PVDF thin film acoustic actuator	12
2.6 Characterization	13

Chapter 3. Results and discussion	14
3.1 Fabrication of PVDF-based thin film acoustic actuator.....	14
3.2 Characterization of Ba-HNPs/PVDF thin film.	23
3.3 Crystallinity of Ba-HNPs/PVDF thin film.....	28
3.4 Permittivity and loss factor of Ba-HNPs/PVDF thin film	37
3.5 Performance of PVDF-based thin film acoustic Actuator using CVD graphene electrode	46
3.5.1 Effect of PVDF film thickness on the acoustic actuator	46
3.5.2 Effect of Ba-HNPs content on sound response in the bass frequency range.....	48
3.5.3 Effect of electrode on the acoustic actuator	53
Chapter 4. Conclusion	57
References	58
Abstract	63

List of Figures

Scheme 1. Fabrication of the Ba–HNPs/PVDF thin film acoustic actuator via electrospinning, hot-pressing, mechanical stretching under high voltage, and transferring CVD-graphene onto the silane- treated thin film. The Ba–HNPs/PVDF-based thin film was synthesized at 220 °C and 800 psi, and the polling and drawing processes were done at 30 kV/cm. The APS coupling agent was used to modify the surface. A sandwich structure having CVD- graphene electrodes was fabricated.	17
Scheme 2. (a) Schematic representation of the interfacial effect of porous Ba–HNPs when enhancing the β phase content. b) Sketch showing the porous structure of the Ba–HNPs having electrically charged surfaces.....	45
Figure 1. EDX spectra of the Ba-HNPs.....	18
Figure 2. STEM-EDX line mapping of the Ba-HNPs.	20
Figure 3. (a) Representation HR-TEM and (b) AFM images of CVD- grown graphene as an electrode. Inset Raman spectra showed D, G and 2D peaks, and the average thickness of graphene was assumed to be ca. 1.9nm.....	21

Figure 4.	Photograph of a Ba-HNPs/PVDF-based thin film acoustic actuator with flexibility and transparency using sandwiched CVD grown graphene electrodes	22
Figure 5.	Representative FTIR spectra of PVDF film by content of Ba-HNPs	26
Figure 6.	DSC thermograms of pristine PVDF and Ba-HNPs/PVDF composites cooled from 190 °C at a cooling rate of 10°C/min ...	32
Figure 7.	Relative crystallinity as a function of time.....	33
Figure 8.	Plot of $\ln[-\ln(1-X_t)]$ versus $\ln t$ for thermal behavior parameters.	34
Figure 9.	Polarized optical microscopy image of (a) pristine PVDF, (b) 10 wt% Ba-HNP/PVDF, (c) 15 wt% Ba-HNP/PVDF, and (d) 20 wt% Ba-HNP/PVDF. All samples were isothermally crystallized at 160 °C for 240 s and repeated 10 times.....	36
Figure 10.	Permittivities and loss factors of Ba–HNPs/PVDF thin films containing various loadings of Ba–HNPs. The loss factor was obtained by differentiation of the permittivity values	42
Figure 11.	Measured (this work) and theoretical (BSP model) permittivity values as a function of filler content at specific frequencies.....	43
Figure 12.	(a) Frequency response and (b) THD value of PVDF thin film with various thickness of ca. 60, 80, 100 and 120 μm	47

Figure 13. Frequency responses of Ba–HNPs/PVDF-based thin film acoustic actuators as a function of Ba–HNPs content.	50
Figure 14. THD values of Ba–HNPs/PVDF-based thin film acoustic actuators as a function of Ba–HNPs content.	51
Figure 15. Relative efficiency of the actuators at 100 Hz as a function of filler content... ..	52
Figure 16. Transmittance of Ba–HNPs/PVDF-based thin film acoustic actuator with three types of electrodes.	55
Figure 17. (a) Frequency responses and (b) THD values for 15 wt% Ba–HNPs/PVDF film with CVD-graphene, rGO, and PEDOT:PSS electrodes.....	56

List of Tables

Table 1.	EDX analysis of Ba-HNPs elemental contents. Since carbon tape was used to hold Ba-HNPs, atom contents of carbon and oxygen were excluded.....	19
Table 2.	β phase content, $F(\beta)$, of pristine PVDF followed by PVDF with various concentration of Ba-HNPs.....	27
Table 3.	Values of n , k and $t_{1/2}$ for pristine PVDF and various concentration of Ba-HNP/PVDF	35
Table 4.	Relevant dielectric parameter for Ba-HNPs/PVDF composite with various filler contents	44

Chapter 1. Introduction

1.1 Flexible Acoustic Actuator

1.1.1 Piezoelectric material

A highly transparent thin-film acoustic actuator using a piezoelectric material has attracted a great deal of interest as a next-generation flexible device due to its low power consumption, light weight, and compact size. Mechanical vibration of thin film can be produced under applied voltage via inverse piezoelectric effect [1]. Among the various piezoelectric materials, poly(vinylidene fluoride) (PVDF) has received considerable attention in the past decade because of its nontoxicity, low cost and density. As a representative semi-crystallin polymer, it has three possible polymorphs such as α (α),

beta(β), and gamma(γ) phases according to the chain conformation of trans and gauche linkages [2-4]. Especially, the piezoelectric property of PVDF is strongly dependent of its β phase content owing to high net dipole moment originates from the all-trans structure [4]. Therefore, a large effort has been devoted to improve β phase content of PVDF for piezoelectric devices in acoustic application[5-8]. However, it is still a challenge to use pristine PVDF as a piezoelectric material for thin film acoustic actuator because it has poor bass sound below 500 Hz.

1.1.2 Nanofiller composite

Martins *et al.* recently introduced ceramic nanofillers into a PVDF matrix to enhance the piezoelectric property [9]. The loading of high dielectric BaTiO₃ nanoparticles improved permittivity of PVDF which is ascribed to increased β phase contents [9,10]. In spite of dielectric fillers leading to high piezoelectricity of PVDF, they have limited the maintenance well-dispersed fillers in matrix. Namely, incorporating high concentration of nanofillers to matrix caused particle–particle aggregation that result in reduction of permittivity [11-14]. For this reason, the ability to control morphology of the nanofiller has been focused on recently in order to fabricate a low density of nanoparticle, such as hollow nanoparticles..

1.1.3 Various electrodes

Using a highly conductive electrode to deliver distortion-free input signals from a sound generator to the surface of the film is also important for a high-quality thin-film acoustic actuator. The graphene, a two-dimensional and single-layer hexagonal lattice of sp^2 -carbon atoms, is considered a potential breakthrough for contact electrode because of its extremely high electron mobility, transmittance, and excellent mechanical strength with flexibility [15-20]. In particular, the reduced graphene oxide (rGO) make advances in high quality mass production at a low-cost [21]. Therefore, in our previous work, rGO was modified as electrodes for flexible acoustic actuator and it was homogeneously deposited by inkjet-printing method. However, there are still needed to increase low conductivity, which lead to a poor frequency response [19]. In this regard, the high conductive chemical vapor deposition (CVD) graphene can make it possible to enhance the performance of film acoustic actuator. Moreover,

uniform low sheet resistance of few layer graphene can transport less distortion audio signals and high transparent [18,19].

1.2 Objective of this study

Herein, we report the behavior of a PVDF thin-film acoustic actuator whose performance of every frequency range has been enhanced by incorporation of Ba-doped $\text{SiO}_2/\text{TiO}_2$ hollow nanoparticles (Ba-HNPs) as nanofiller and graphene electrodes grown by CVD. Importantly, a high concentration of monodisperse Ba-HNPs in the PVDF matrix (Ba-HNPs/PVDF) was successfully fabricated as a nucleation agent, and improved piezoelectricity PVDF was easily prepared at large scale via electrospinning [22,23]. To gain insight into PVDF properties according to contents of fillers, the investigation was divided into two respects, crystalline behavior and parameters of permittivities. Furthermore, we applied PVDF-based thin film for practical acoustic actuator to demonstrate frequency response and total harmonic distortion (THD) as a function of concentration of nanofiller and various electrode types. To the best of

our knowledge, this is the first experimental evidence for a bass frequency range enhanced thin-film acoustic actuator relative to content of β phase PVDF.

Chapter 2. Experimental

2.1 Materials

Tetraethyl orthosilicate and titanium (IV) isopropoxide (TTIP, Sigma-Aldrich Chemical Co., USA) and a centrifuge (Mega 17R, Hanil Science and Industrial, South Korea) were used to fabricate the Ba-HNPs. The graphite used in the experiments was purchased from Sigma-Aldrich. Graphene electrodes were printed using a commercial office inkjet printer (Canon Pixima Ip1300). Gases (H_2 , CH_4 , Ar; 99.99%; Daesung Industrial Gases Co., South Korea), Cu foil (Sigma-Aldrich), and poly(methylmethacrylate) (950 PMMA A4, 4% in anisole, MicroChem Corp., USA) were used in the fabrication of the graphene films. PVDF pellets (molecular weight *ca.* 275,000 by gel permeation chromatography), (3-aminopropyl)trimethoxysilane (APS), and DMF were obtained from Sigma-Aldrich. Commercial PVDF film was obtained from the Fils Corporation (South Korea).

2.2 Synthesis of Ba-doped SiO₂/TiO₂

First, 475 mL of ethanol and 17.4 mL of aqueous ammonia were mixed with 17.4 mL of tetraethyl orthosilicate for 12 h at 60°C. Acetonitrile (175 mL) was then added to form a colloidal SiO₂ solution. Second, 21.6 mL of TTIP, 108 mL of ethanol, and 36 mL of acetonitrile were added to the colloidal SiO₂ solution at 5°C, and the mixture was stirred for 12 h. The resulting SiO₂/TiO₂ core/shell nanoparticles precipitated and were isolated by centrifugation. These nanoparticles were resuspended in 500 mL of aqueous Ba(OH)₂ solution, which was sonicated for 3 h to disperse the particles. Finally, SiO₂ was etched under basic conditions. The resulting Ba-HNPs were isolated by centrifugation, redispersed in deionized water, and dried in a vacuum oven at 60 °C.

2.3 Preparation of the Ba-HNPs/PVDF thin film

PVDF was dissolved in a 1:1 mixture of DMF, and acetone and Ba-HNPs were added to it. The mixture was sonicated for 2 h to disperse the particles. The solution was transferred into a 12-mL-capacity syringe pump and a 15 kV/cm high voltage was applied between stainless steel plates. The solution was injected onto the collector plate at a constant flow rate of 75 $\mu\text{m}/\text{min}$ using the electrospinning process. Ba-HNP/PVDF nanocomposite fiber was collected on a polyimide film at room temperature and was dried at 60 $^{\circ}\text{C}$ in a vacuum oven for 12 h. The dried spun Ba-HNPs/PVDF nanofiber mat on the polyimide film was pressed at 220 $^{\circ}\text{C}$ and 800 psi for 1 h and then slowly cooled. The fabricated Ba-HNP/PVDF films were uniaxially drawn at 10 mm/min to maximize the α -to- β phase transformation; drawing was continued until the film reached 200 % of its original length at 90 $^{\circ}\text{C}$ while polling was done under a strong constant electric field at 30 kV/mm.

2.4 Preparation of CVD-grown graphene electrode

Cu foil ($7 \times 7 \text{ cm}^2$) was placed in a glass chamber, and then heated to 1000°C under an 8-sccm flow rate of H_2 gas at 90 mTorr. This condition was maintained for 30 min to condition the inner surface of the glass chamber. Then, a 20 sccm flow of CH_4 gas was drawn into the glass chamber to a total pressure of 560 mTorr, which was held for 40 min. The chamber was then cooled to room temperature at $35^\circ\text{C}/\text{min}$ under a H_2 atmosphere. The solution (4%) of PMMA in anisole was spin-coated at 5,000 rpm for 1 min onto the Cu foil. The pristine graphene was isolated after immersing the coated foil into Cu etchant.

2.5 Fabrication of the Ba-HNPs/PVDF thin film acoustic actuator

Ba-HNP/PVDF film ($7 \times 7 \text{ cm}^2$) was treated with a 0.5 wt% aqueous APS solution for 12 h to render the surface hydrophilic. The film was then dried at 60 °C for 6 h. A sandwich structure was fabricated that consisted of the Ba-HNP/PVDF film sandwiched between CVD-grown graphene/PMMA films. The PMMA was removed from the graphene by dissolving in chloroform.

2.6 Characterization

High-resolution TEM images were taken using a JEOL JEM-3010 instrument. Field-emission scanning electron microscopy (FE-SEM, JEOL JSM-6700F, Japan) and a FTIR spectrometer (Bomem MB 100, USA) were also used. Atomic force microscopy (AFM, Nanoscope IIIa, Digital instruments, USA) was used to image the surface topography; it was used in the tapping mode with silicon tips at a resonance frequency of 320 kHz. Electrical resistances were measured with a Keithley 2400 source meter at 25 °C using the four-probe method. Raman spectra were recorded on a LabRAM HR (Horiba, Japan) with 1064-nm laser excitation. A dScope Series IIIA (Prism Sound Co., UK) audio analyzer was used to determine the acoustic actuator characteristics from 10 Hz to 20 kHz.

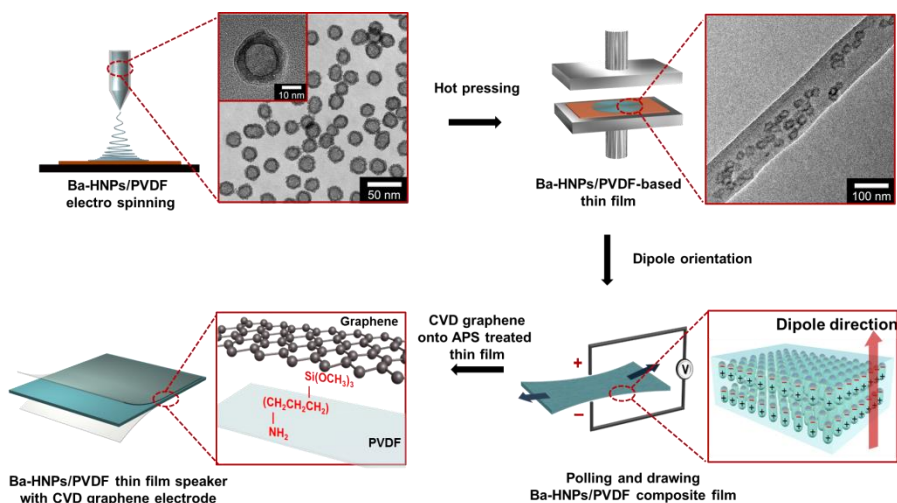
Chapter 3. Results and discussion

3.1 Fabrication of PVDF-based thin film acoustic actuator

The overall procedure for the fabrication of the graphene-based Ba–HNPs/PVDF acoustic actuator is illustrated in Scheme 1. Electrospinning was used to introduce the Ba–HNPs into the PVDF matrix ; Drop casting and spin coating meathod hindered to embed monodispersed Ba–HNPs at large-scale. First, the Ba–HNPs were synthesized according to Stöber’s method [24]. Energy-dispersive X-ray (EDX) analysis showed the presence of Ba, Ti, Si, and O from the filler (Figure 1 and Table 1). The Ba–HNPs were reasonably monodisperse and their average diameter was *ca.* 20 nm (Scheme 1 insert, top-left transmission electron microscopy (TEM) image and Figure 2). The prepared Ba–HNPs were mixed into a solution of

PVDF, which was then electrospun to form a Ba–HNPs/PVDF mat. The mat was placed on a hot press and pressed into a homogeneous film. Ba–HNPs could be seen on a spun PVDF fiber (Scheme 1, top-right TEM image). Polling and drawing provided high transparency and polarization. Subsequently, an acoustic actuator electrode was constructed from a large ($7 \times 7 \text{ cm}^2$) film of 1.9-nm-thick CVD-graphene that consisted of a few layers of low-defect graphene (Figures 3 a and b). The surface of the fabricated thin film was treated with 3-aminopropyltriethoxysilane (APS) coupling agent to improve adhesion to the graphene electrode; reaction occurred between the $-\text{OCH}_2\text{CH}_3$ groups of APS with oxygen-containing functional groups such as $-\text{OH}$ on the surface of the synthesized CVD-graphene [26]. Additionally, the terminal $-\text{NH}_2$ groups of APS reacted with the fluorine atoms of PVDF to form F–H bonds. Hence, the acoustic actuator consisted of a sandwich of a Ba–HNPs/PVDF thin film and

CVD-graphene electrodes, which was connected to a sound source and amplifier (Figure 4).



Scheme 1. Fabrication of the Ba–HNPs/PVDF thin film acoustic actuator *via* electrospinning, hot-pressing, mechanical stretching under high voltage, and transferring CVD-graphene onto the silane-treated thin film. The Ba–HNPs/PVDF-based thin film was synthesized at 220 °C and 800 psi, and the polling and drawing processes were done at 30 kV/cm. The APS coupling agent was used to modify the surface. A sandwich structure having CVD-graphene electrodes was fabricated.

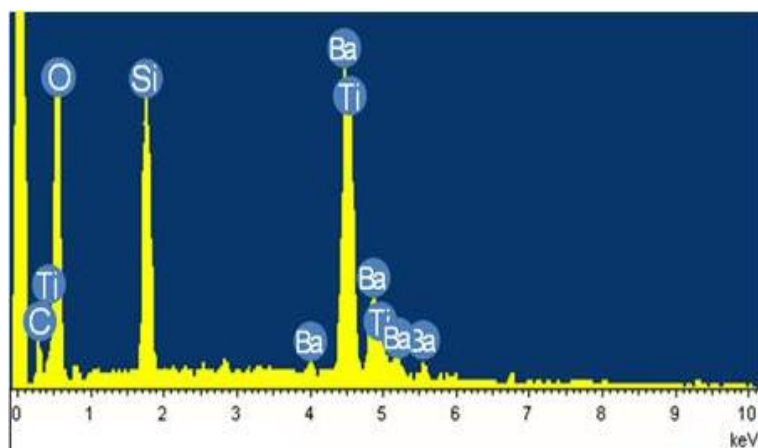


Figure 1. EDX spectra of the Ba-HNPs.

Table 1. EDX analysis of Ba-HNPs elemental contents. Since carbon tape was used to hold Ba-HNPs, atom contents of carbon and oxygen were excluded.

Sample	Ti /atomic %	Ba /atomic %	Si /atomic %
Ba-HNPs	36.04	34.85	29.11

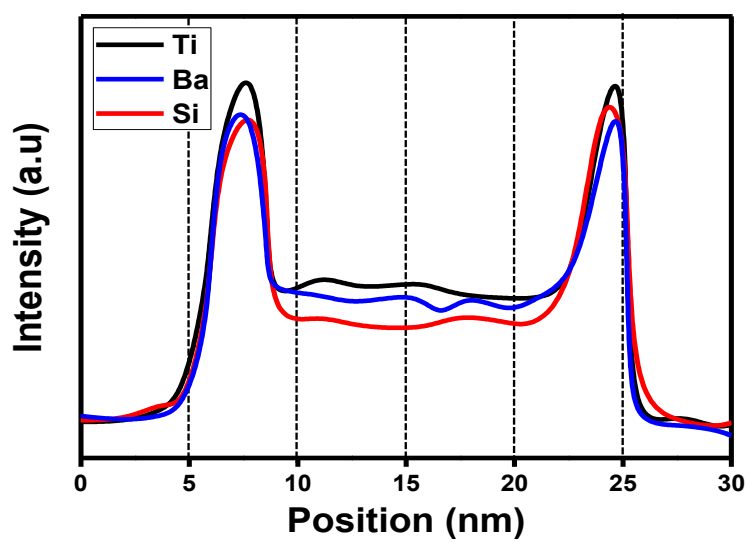


Figure 2. STEM-EDX line mapping of the Ba-HNPs.

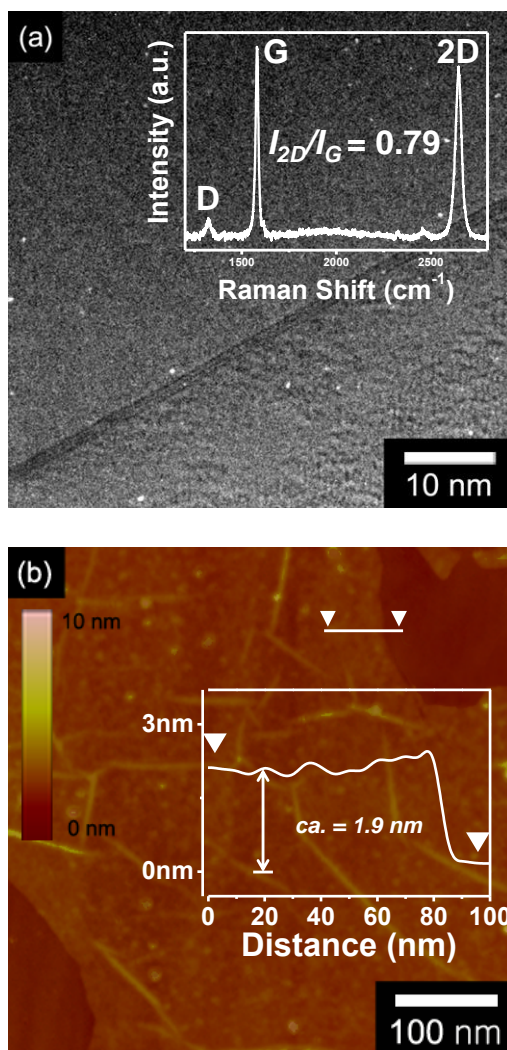


Figure 3. (a) Representation HR-TEM and (b) AFM images of CVD-grown graphene as an electrode. Inset Raman spectra showed D, G and 2D peaks, and the average thickness of graphene was assumed to be *ca.* 1.9nm.

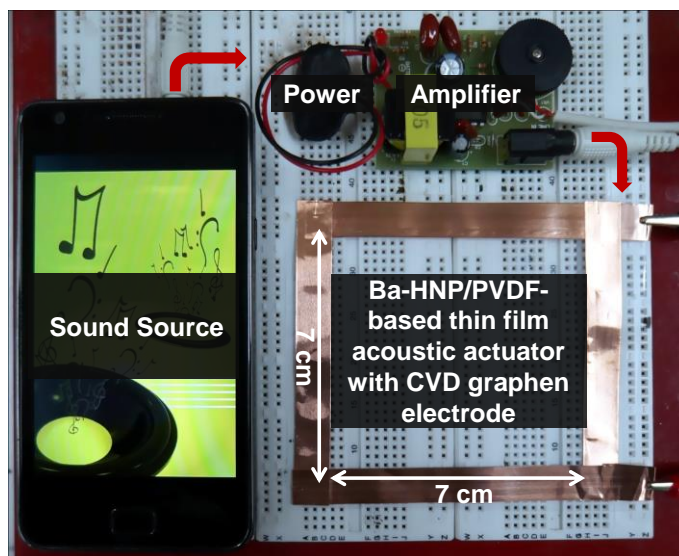


Figure 4. Photograph of a Ba-HNPs/PVDF-based thin film acoustic actuator with flexibility and transparency using sandwiched CVD grown graphene electrodes.

3.2 Characterization of Ba-HNPs/PVDF thin film

Figure 5 and 6 show the Fourier transform infrared (FTIR) spectrum and differential scanning calorimetry (DSC) of PVDF, which was used to investigate the crystallization behavior during the fabrication of the PVDF thin film and the effect of incorporating Ba-HNPs into the film. Figure 5 shows the changes in the crystalline α and β phase contents by contents of filler [26,27]. The α phase of PVDF is composed of repeating 1,1-difluoroethyl units joined to CF_2 groups in a *trans-gauche* configuration. The skeletal bending vibrations of the α phase appeared at 615, 766, and 974 cm^{-1} . The β crystalline phase has an *all-trans* conformation, which is a planar zigzag configuration whose $\text{CH}_2\text{--CF}_2$ rocking and asymmetric stretching modes are absorbed at 840 and 1275 cm^{-1} . Furthermore, the β phase content in PVDF was estimated assuming that the FTIR absorptions followed the Lambert–Beer law (Supporting Information) [28]. The γ and δ phase contents were neglected in this calculation because of their small quantities in the composite samples. The

pristine PVDF film had a β phase content of 79 %. Most of all, the changes in β phase induced by the addition of the Ba–HNPs are also shown in Figure 5 and Table 2 summarizes the findings. Adding 10 wt% of the Ba–HNPs led to an I_{β}/I_{α} of *ca.* 2.37 and was 87 % β phase, and incorporating 15 wt% Ba–HNPs led to an I_{β}/I_{α} of *ca.* 2.56 with 95 % β phase. However, for 20 wt% loading, the I_{β}/I_{α} value decreased to *ca.* 2.38 or 89 % β content because of exceeding saturation content of Ba-HNPs limited dispersion of fillers. Judging from this data, electrospinning method can easily provide polling and drawing effects to enhance ratio of β phase compare to drop casting and spin coating method. Furthermore, the β phase content in PVDF was estimated assuming that the FTIR absorptions followed the Lambert–Beer law.

Assuming the IR absorption follows the Lambert-Beer law, content of β phase in PVDF can be measured,

$$F(\beta) = \frac{X_\beta}{X_\alpha + X_\beta} = \frac{A_\beta}{(K_\beta/K_\alpha) + A_\beta} \quad (1)$$

Where A_α and A_β are the absorbance at 766 and 840 cm^{-1} respectively, and K_α ($6.1 \times 10^4 \text{ cm}^2/\text{mol}$) and K_β ($7.7 \times 10^4 \text{ cm}^2/\text{mol}$) are the absorption coefficients at the respective wavenumber.

The γ and δ phase contents were neglected in this calculation because of their small quantities in the composite samples. Table 2 summarizes the estimated β phase contents. The electrospun pure PVDF mat had 76 % β phase content while the hot-pressed PVDF film had only 19 %. However, the dipole-orientated PVDF film had a high β phase content of 79 %.

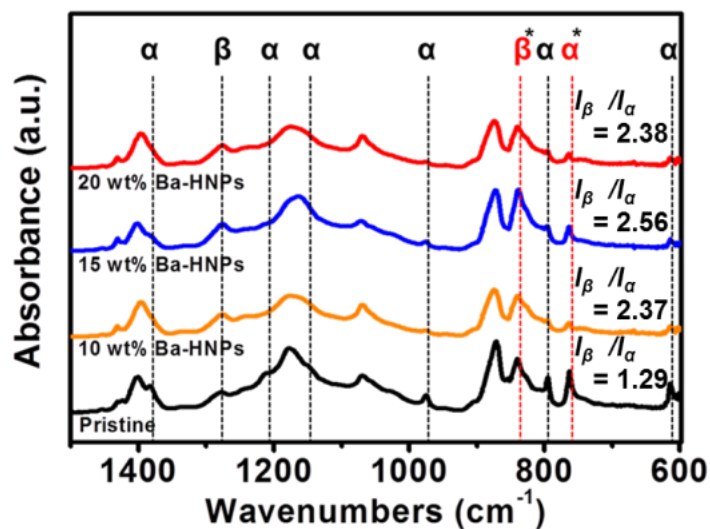


Figure 5. Representative FTIR spectra of PVDF film by contents of Ba-HNPs.

Table 2. β phase content, $F(\beta)$, of pristine PVDF followed by PVDF with various concentration of Ba-HNPs.

Sample	$F(\beta)$ (%) [a]
Pristine PVDF	79
10 wt% Ba-HNP/PVDF	87
15 wt% Ba-HNP/PVDF	95
20 wt% Ba-HNP/PVDF	89

[a] These values were calculated by Lambert-Beer law.

3.3 Crystallinity of Ba-HNPs/PVDF thin film

To achieve an in-depth insight into the crystallization behavior by filler concentration, DSC analysis was conducted. Figure 6 indicates the DSC thermograms of pristine PVDF and Ba-HNPs obtained at a cooling rate of 10 °C/min. The observed crystallization exothermic peak are observed in the range of 160 to 170 °C and it was confirmed the role of Ba-HNPs as nucleation agents of PVDF according to increase of crystallization temperature (T_c) compare to pristine PVDF [29]. The relative degree of crystallinity as a function of time, $X(t)$, can be calculated from relative crystallinity as a function of temperature, $X(T)$, by transforming the temperature to a time scale (Figure 7) [30]. It shows crystallinity of PVDF is most rapidly formed at 15 wt% of Ba-HNPs.

The relative degree of crystallinity as a function of time, $X(t)$, can be calculated from relative crystallinity as a function of

temperature, $X(T)$, by transforming the temperature to a time scale. In this manner, the relative degree of crystallinity was plotted by equation below (Figure 7).

$$X(t) = \frac{\int_0^t \left(\frac{dH}{dt}\right) dt}{\int_0^\infty \left(\frac{dH}{dt}\right) dt} = \frac{A_t}{A_\infty} \quad (2)$$

Where numerator, A_t , is the area under DSC curve from $t = 0$ to t and denominator, A_∞ , is the total area under the crystallization curve.

Additionally, natural logarithmic form of Ozawa equation was used to investigate non-isothermal crystallization of kinetics by considering the cooling rate. Figure 8 indicates a double logarithmic plot of $\ln[-\ln(1-X_t)]$ verse $\ln t$ for each samples.

Natural logarithmic form of Ozawa equation was used to investigate non-isothermal crystallization of kinetics by considering the cooling rate.

$$\ln[-\ln(1 - X_t)] = \ln k + n \ln t \quad (3)$$

Where X_t the temperature-dependent relative crystallinity, t is the

duration of the crystallization, k is the constant of crystallization rate and n is the Ozawa exponent.

Especially, highest crystallization rate constant (k) of 0.05448 was obtained with 15 wt% and values of Ozawa exponent (n), 2.016 and reaching half-time crystallinity ($t_{1/2}$), 1.694 μ s and it is summarized in Table 3. The values of the crystallization rate increase with contents of Ba-HNPs until the 15 wt% as expected, but when concentration of filler exceeded 20 wt % caused decreasing value. Moreover, it observed same tendency from crystallization half-time. In other word, it was demonstrated that showing highest crystallization rate of 15 wt% Ba-HNPs/PVDF implies fastest crystallization growth time.

This indicates that addition of Ba-HNPs into PVDF matrix has an effect on the crystal structure. Figure 9 shows that observed polarized optical microscopy morphology (POM) of the crystal growth. All samples were isothermally crystallized at 170 °C and maintained for

240 s, and it was repeated 10 times to observe crystal growth tendency. After it cooled down, same procedure was repeated 10 times to obtain accurate tendency of crystal growth morphology [31]. The amounts of spherulites were significantly increased by loading concentration of Ba-HNPs. It means that added Ba-HNPs act as nuclei for PVDF crystallization and alter the kinetics of crystallization at constant time. According to the charge-charge interaction of Ba-HNPs and with $-\text{CF}_2$ dipole, α crystalline PVDF chains have converted to trans-trans conformation [4]. As a result, reinforced crystallization behavior is intimately proportional to content of β phase..

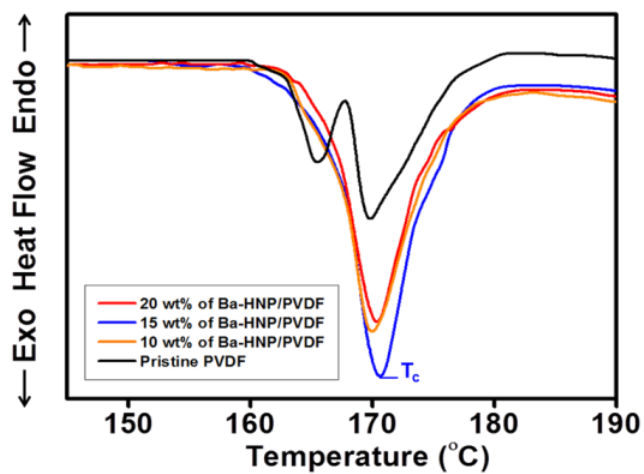


Figure 6. DSC thermograms of pristine PVDF and Ba-HNPs/PVDF composites cooled from 190 °C at a cooling rate of 10°C/min.

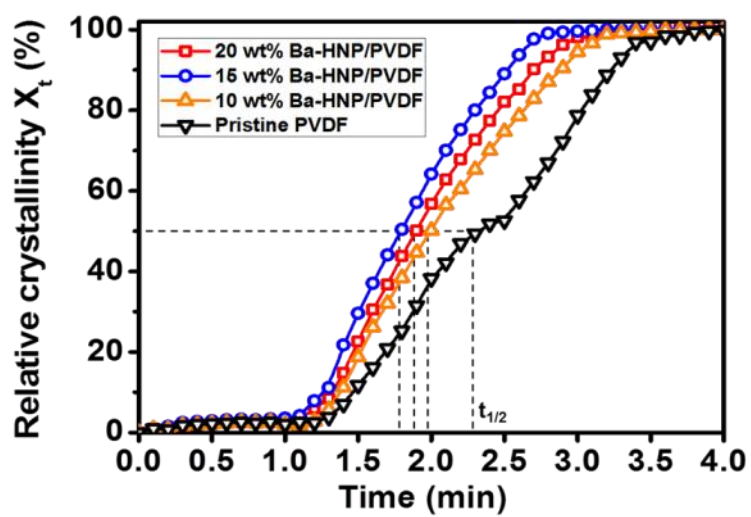


Figure 7. Relative crystallinity as a function of time.

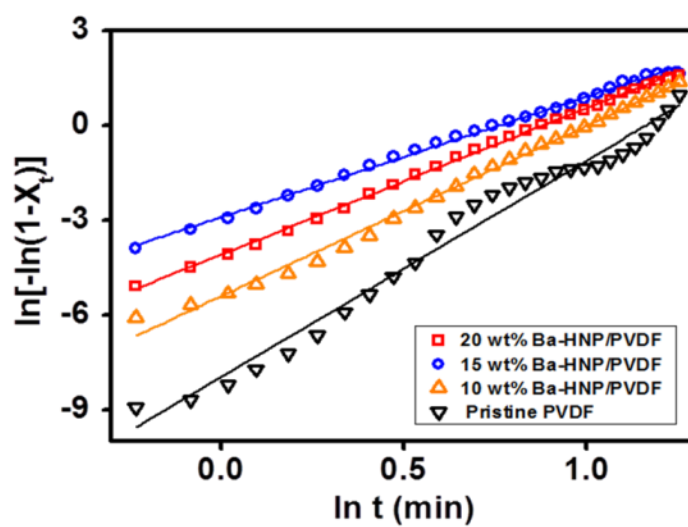


Figure 8. Plot of $\ln[-\ln(1-X_t)]$ versus $\ln t$ for thermal behavior parameters.

Table 3. Values of n , k and $t_{1/2}$ for pristine PVDF and various concentration of Ba-HNP/PVDF.

Sample	n [a]	k [a]	$t_{1/2}$ (min) [a]	T^{β}_c (°C)
Pristine PVDF	3.004	0.00035	2.301	170.15
10 wt% Ba-HNP/PVDF	2.624	0.00447	1.946	170.13
15 wt% Ba-HNP/PVDF	2.016	0.05448	1.694	170.91
20 wt% Ba-HNP/PVDF	2.572	0.01667	1.813	170.16

[a] These values were obtained by Ozawa analysis of samples using DSC.

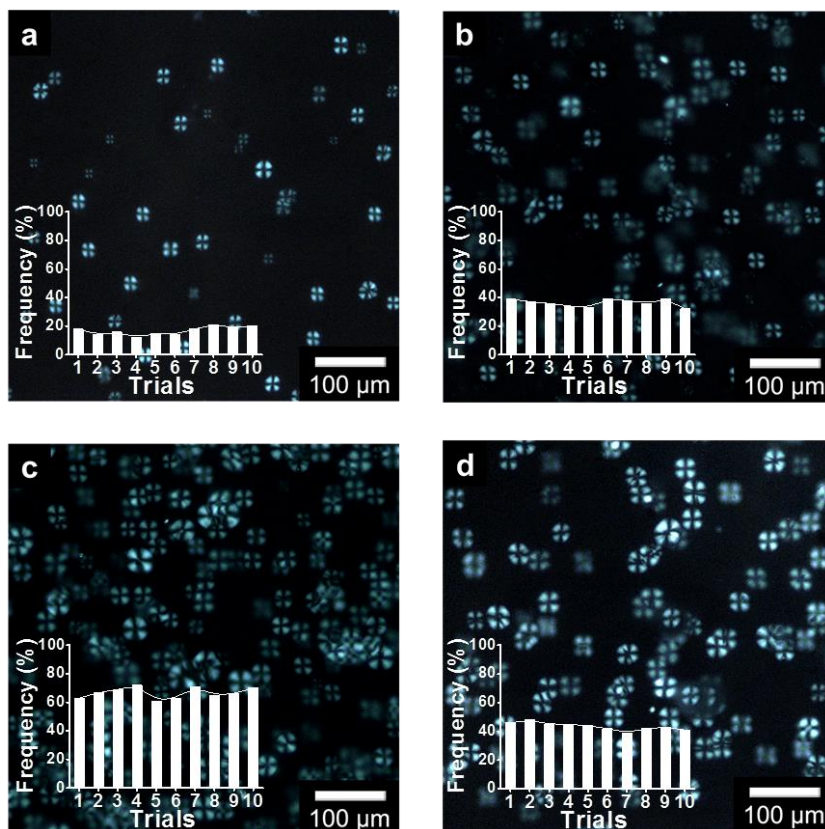


Figure 9. Polarized optical microscopy image of a) pristine PVDF, b) 10 wt% Ba-HNP/PVDF, c) 15 wt% Ba-HNP/PVDF, and d) 20 wt% Ba-HNP/PVDF. All samples were isothermally crystallized at 160 °C for 240 s and repeated 10 times.

3.4 Permittivity and loss factor of Ba-HNPs/PVDF thin film

In general, the β phase PVDF is highly ferroelectric and piezoelectric because every dipole points in the same direction. Therefore, the permittivity and loss factor of the fabricated Ba-HNPs/PVDF-based thin film were determined as a function of filler content. The measured permittivity at has few trend that lower frequencies always greater than at higher frequencies and increasing the loading of Ba-HNPs significantly increased the dielectric constant (Figure 10). Additionally, the range of relaxation slopes (α_a) are mainly overlapped at 1 kHz; it represents the reversible conformational rearrangements and chain-folding of the crystalline lamellae in the interior of the PVDF [32,33]. Figure 11 shows that the experimental dielectric constant was similar to that based on the theoretical model of Bhimasankaram *et al.* (BSP) [34].

Dielectric constant value on theoretical model of Bhimasankaram, is defined as

$$\varepsilon = \frac{\varepsilon_1(1-\Phi) + \varepsilon_2\Phi[3\varepsilon_1/(\varepsilon_2+2\varepsilon_1)][1+3\Phi(\varepsilon_2-\varepsilon_1)(\varepsilon_2+2\varepsilon_1)]}{(1-\Phi) + [\Phi(3\varepsilon_1)/\varepsilon_2+2\varepsilon_1][1+3\Phi(\varepsilon_2-\varepsilon_1)(\varepsilon_2+2\varepsilon_1)]} \quad (4)$$

where ε_1 is the dielectric constant of the PVDF, ε_2 is the dielectric constant of the filler, and Φ is the volume fraction of filler, calculated in Table 4.

The BSP model evaluates dipoles that are locally modified and aligned in the direction of the applied electric field in the near region. This result indicated that the Ba-HNPs played a pivotal role in the permittivity properties of the PVDF. Furthermore, electrical response was studied to better understand the space charge at the interface of the filler and the PVDF polymer. The proper interfacial polarization responses are denoted by relaxation time, λ at 10 kHz. The values of permittivities (ε') and dielectric strengths ($\Delta\varepsilon$) were reinforced by loading Ba-HNPs concentration increased, also relaxation times were

shorten (Table 4). The value was estimated using the Havriliak–Negami and Fourier transforms relationship. As a result, polarizability was enhanced by the addition of Ba–HNPs. Considering this results, it could be inferred that the permittivity was enhanced because of the space charge interaction in PVDF at the interface with the Ba–HNPs.

Polarizability by addition of Ba-HNPs filler can be estimated by Havriliak-Negami and Fourier transfer relationship,

$$\varepsilon^* = \varepsilon' + i\varepsilon'' = \varepsilon_\infty + \frac{\Delta\varepsilon}{1+(i\omega\lambda)^{1-\alpha}} \quad (5)$$

Where ε' is dielectric constant, ε'' is the dielectric loss factor,

therefore, Polarizability is defined as,

$$\Delta\varepsilon = \varepsilon_S - \varepsilon_\infty \quad (6)$$

ε_S is ε' as $\lim_{\omega \rightarrow 0} \varepsilon^*(\omega)$, and ε_∞ is ε' as $\lim_{\omega \rightarrow \infty} \varepsilon^*(\omega)$,

calculated in table 4.

The proper interfacial polarization responses are denoted by relaxation time, λ .

Proper interfacial polarization response by relaxation time, is defined as

$$\lambda = \frac{1}{2\pi f_{max}} \quad (7)$$

Where f_{max} is the frequency of the loss peak, calculated in Table 4.

Furthermore, when PVDF powder was dissolved in N,N-dimethylformamide and acetone, strong hydrogen bonds such as O–H···F–C were formed because of the high polarity of the hydroxyl groups (C=O and CH₂–CF₂ dipoles). This favored the β -phase configuration of the CH₂–CF₂ entity [2]. The dielectric values were proportionally enhanced to Ba-HNPs concentration until loading contents of 15 wt% compare to 20 wt%. Although decreased β phase

contents of 20 wt% compare to 15 wt%, the permittivity values were slightly enhanced. Considering these results, it can be deduced that interfacial on porous shell of Ba-HNPs charges can make it possible to increase piezoelectricity. Scheme 2 illustrates how the porous structure of the Ba-HNPs can facilitate transportation of charge by modifying the arrangement of the charges [26]. The ferroelectric phase is strongly influenced by the geometry of the fillers through the interfacial interaction between the local electric field of the filler and the PVDF dipoles. Consequently, increasing the filler content enhanced the piezoelectric potentials, and decreasing the filler particle size increased the surface area, which also contributed to elevating the permittivity.

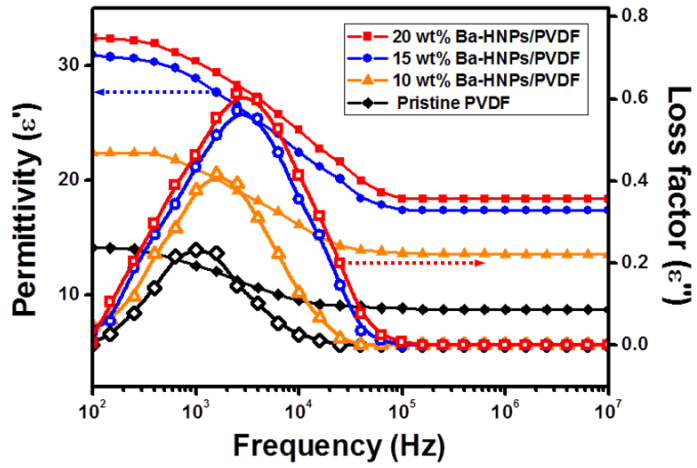


Figure 10. Permittivities and loss factors of Ba–HNPs/PVDF thin films containing various loadings of Ba–HNPs. The loss factor was obtained by differentiation of the permittivity values

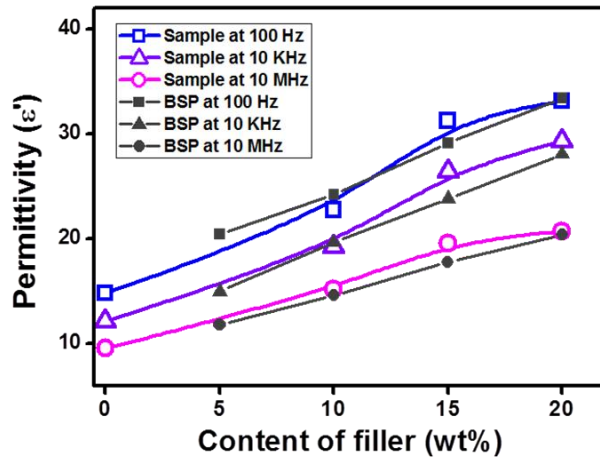


Figure 11. Measured (this work) and theoretical (BSP model) permittivity values as a function of filler content at specific frequencies

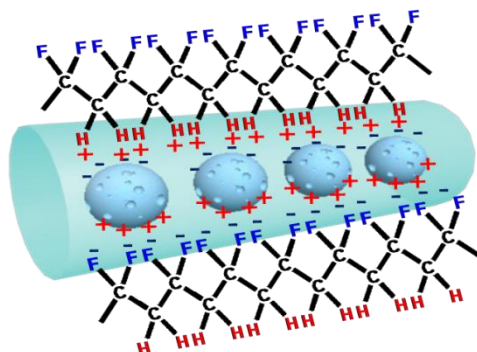
Table 4. Relevant dielectric parameter for Ba-HNPs/PVDF composite with various filler contents.

Sample	ϵ' [a]	$\Delta\epsilon$ [a]	λ [μ s] [b]
Pristine PVDF thin film	11	4.9	159
10 wt% Ba-HNP/PVDF	16	5.3	80
15 wt% Ba-HNP/PVDF	21	8.1	62
20 wt% Ba-HNP/PVDF	22	8.8	67

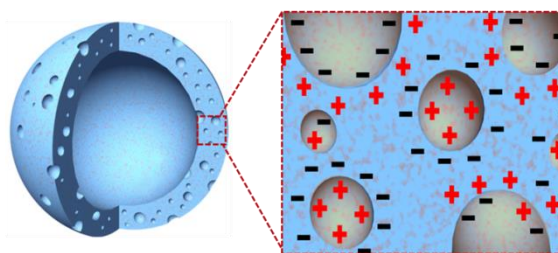
[a] Values were calculated by Havriliak-Negami and Fourier transforms relationship

[b] Values were obtained by interfacial polarization response by relaxation time.

a)



b)



Scheme 2. (a) Schematic representation of the interfacial effect of porous Ba-HNPs when enhancing the β phase content. (b) Sketch showing the porous structure of the Ba-HNPs having electrically charged surfaces.

3.5 Performance of PVDF-based thin film acoustic Actuator using CVD graphene electrode

3.5.1 Effect of PVDF film thickness on the acoustic actuator

The thickness of the pure PVDF film was also controlled to optimize the performance of the acoustic actuator (Figure 12). As a result, the bass-range frequency response proportionally improved as the thickness of the film increased because of enhanced lengthwise polarizability. However, the treble and midrange sound levels were lower because the thicker film obstructed expansion and contraction. The THD values increased because the increased film thickness restricted oscillation of the film surface. The optimized thickness of the fabricated film was found to be *ca.* 80 μm .

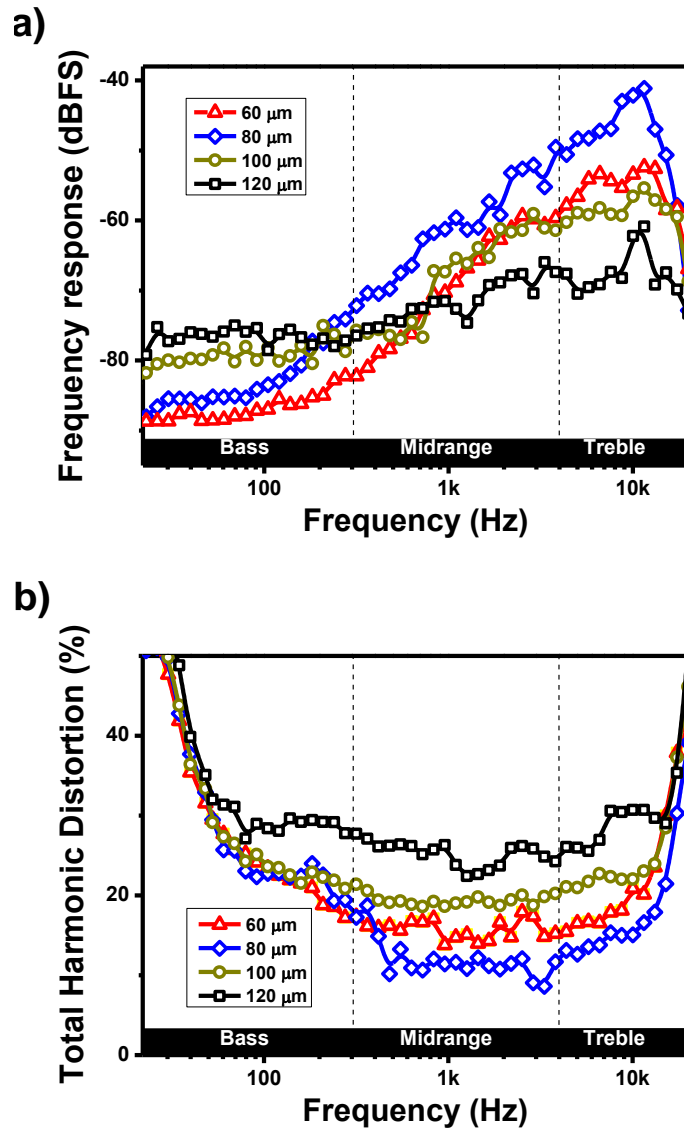


Figure 12. (a) Frequency response and (b) THD value of PVDF thin film with various thickness of *ca.* 60, 80, 100 and 120 μm .

3.5.2 Effect of Ba-HNPs content on sound response in the bass frequency range

Figure 13 illustrates the acoustic performance as a function of dielectric constant and β phase content, and compares it with that of a pristine PVDF film. As a result, loading the Ba–HNPs content in our Ba–HNPs/PVDF heterogeneous thin film improved the overall frequency response. Especially, the sound level of the 10 wt% Ba–HNPs/PVDF film increased by about 18 % in the bass range primarily. Notably, loading with 15 wt% of filler maximized the bass frequency response to 60 %, which was approximately a 20 dB full-scale increase in the sound level. However, it was only enhanced by about 18 % for samples containing 20 wt%. Figure 14 shows the total harmonic distortion (THD) in the bass frequency range with different Ba–HNPs concentration, and the effect of filler content on the frequency response and THD at 100 Hz were suggested (Figure 15) .

The behavior of the THD showed simually improved like frequency response and it ahs decreased by 25 % of THD value with 15 wt% filler content. It showed clear evident that 15 wt% of Ba-HNPs in PVDF was optimum for the thin-film acoustic actuator for maximum sound performance as represented by the frequency response with stable distortion. Importantly, this is the first report demonstrating that content of β phase plays key role the improvement of acoustic performance of PVDF-based thin film. Moreover, the acoustic response of the thin film made with the three different electrodes such as PEDOT:PSS, reduced graphene oxide (rGO), and CVD graphene electrode were investigated.

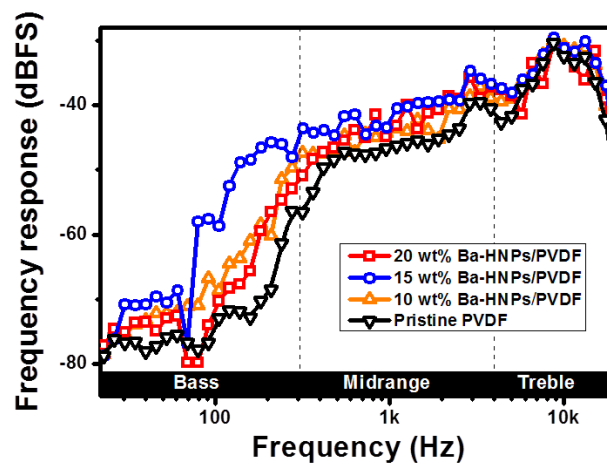


Figure 13. Frequency responses of Ba–HNPs/PVDF-based thin film acoustic actuators as a function of Ba–HNPs content.

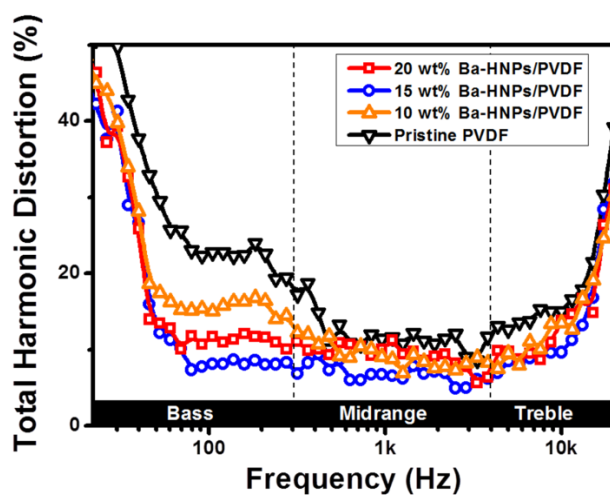


Figure 14. THD values of Ba-HNPs/PVDF-based thin film acoustic actuators as a function of Ba-HNPs content.

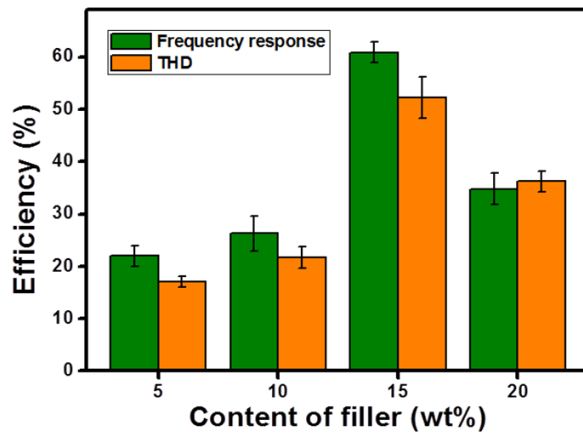


Figure 15. Relative efficiency of the actuators at 100 Hz as a function of filler content.

3.5.3 Effect of electrode on the acoustic actuator

Previous work by Shin *et al.* showed that a lower surface resistance of an electrode affected higher charge carriers and the dipole moment of ferroelectric PVDF [19]. Moreover, using an rGO electrode enhanced the performance of an acoustic actuator at the middle and treble frequency ranges and reduced the power consumption. To confirm the function of the electrode, various electrodes were applied to 15 wt% Ba-HNPs/ PVDF thin film. The sheet resistances of PEDOT:PSS and rGO were 726 and 10 $\text{k}\Omega \text{ sq}^{-1}$, respectively. The CVD-graphene had a sheet resistance of 937 $\Omega \text{ sq}^{-1}$ and *ca.* 95% of the maximum transmittance at about 550 nm (Figure 16)

Figure 17a shows the acoustic response of the thin film made with the three different electrodes was investigated. The performance of the CVD-graphene-based acoustic actuator was 6 % and 17 %

better in the middle and treble frequency ranges, respectively, than that of the modified rGO electrode. Moreover, the CVD-graphene electrode acoustic actuator had 19 % and 22 % higher response in the midrange and treble frequencies, respectively, than a thin-film acoustic actuator with a PEDOT:PSS electrode [6]. Significantly, the CVD electrode could produce a sound level that was at least 4.2 times higher. Additionally, the total harmonic distortion (THD) value of the CVD-graphene-based acoustic actuator was 21 and 17 % lower in the midrange and treble frequencies, respectively (Figure 17b).

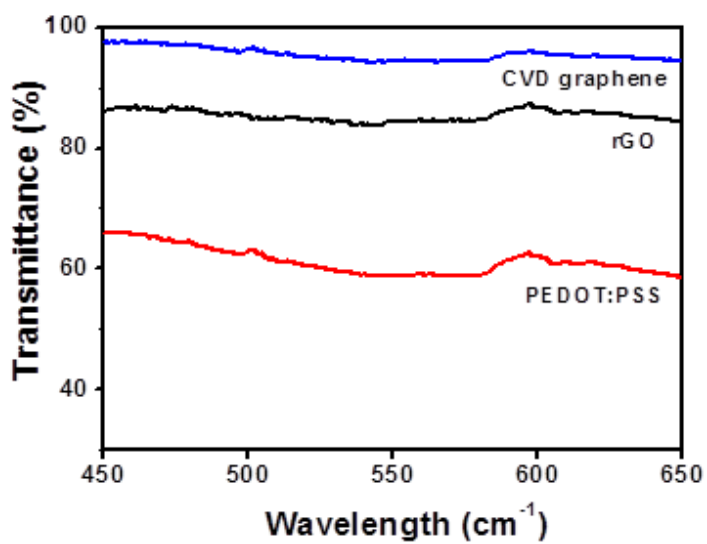


Figure 16. Transmittance of Ba-HNPs/PVDF-based thin film acoustic actuator with three types of electrodes.

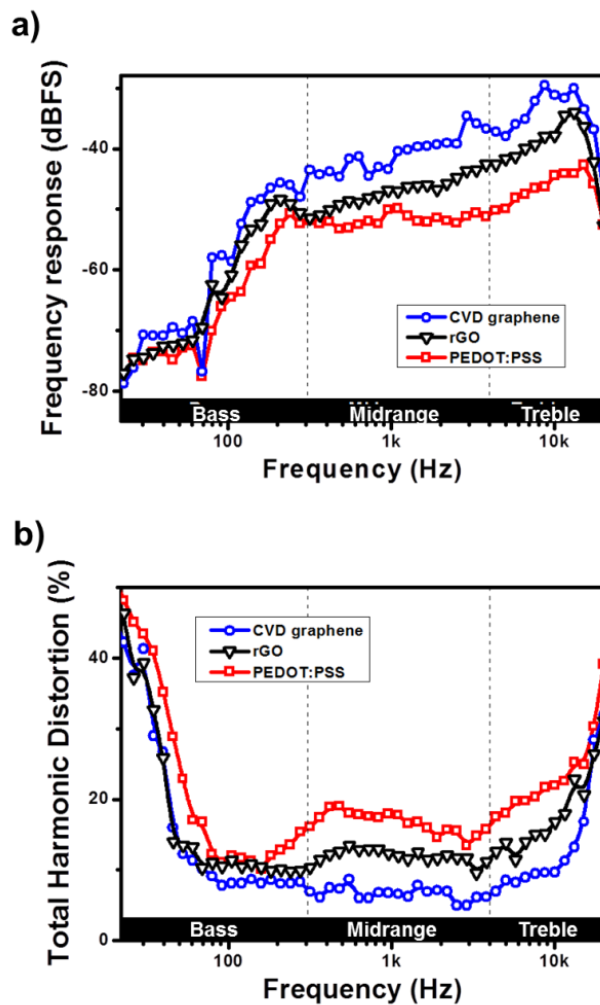


Figure 17. (a) Frequency responses and (b) THD values for 15 wt% Ba-HNPs/PVDF film with CVD-graphene, rGO, and PEDOT:PSS electrodes.

Chapter 4. Conclusion

In conclusion, we have demonstrated that incorporating Ba-HNPs with PVDF and using a CVD-graphene electrode is an effective way to enhance the acoustic performance of a PVDF-based thin-film acoustic actuator. Most of all, it is confirmed that high degree of crystallinity of PVDF strongly effected low bass sound improve. This results implied a 60 % increase in frequency response and 25 % improvement in THD in the bass frequency range by incorporating 15 wt% Ba-HNPs. Furthermore, to deliver a frequency signal rapidly onto the PVDF film surface, high conductivity CVD graphene was used as an electrode and it enhanced acoustic performance at middle and treble ranges with excellent transmittance. This superior performance of the fabricated thin film acoustic actuator has great possibilities for future-oriented applications.

References

- [1] Bea, S. H.; Kahya, O.; Sharma, B. K.; Kwon, J.; Cho, H. J.; Özyilmaz, B.; Ahn, J. H. *Nano Lett.* **2013**, *7*, 3130-3138.
- [2] Wang, S.; Lin, L.; Wang, Z. L. *Nano Lett.* **2012**, *12*, 6339-6346.
- [3] Calvert, P. *Nature*, **1975**, *256*, 694.
- [4] Lovinger, A. J. *Science*, **1983**, *220*, 1115-1121.
- [5] Tiwari, V. K.; Avasthi, D. K.; Maiti, P. *ACS Appl. Mater. Interfaces*, **2011**, *3*, 1398–1401
- [6] Bruna da Silva, A.; Wisniewski, C.; Esteves, J. V. A.; Gregorio Jr, R.. *J Mater Sci.*, **2010**, *45*, 4206-4215.
- [7] Koval, V.; Briancin, J. Effect of Poling Process on the Piezoelectric and Dielectric Properties of Nb and Sr-Doped PZT Ceramics. *Ferroelectrics*, **1997**, *193*, 41-49.

- [8] Yu, S.; Zheng, W.; Yu, W.; Zhang, W.; Jiang, Q.; Zhao, Z. *Macromolecules*. **2009**, *42*, 8870-8874.
- [9] Martins, P.; Lanceros-Mendez, S. *J. Phys. Chem. C*. **2012**, *116*, 15790-15794.
- [10] Martins, P.; Caparros, C.; Gonçalves, R.; Martins, P. M.; Benelmekki, M.; Botelho, G.; Lanceros-Mendez, S. *J. Phys. Chem. C*, **2012**, *116*, 15790-15794.
- [11] Verduyn, M.; Sefcik, J.; Storti, G.; Morbidelli, M. *Polymer Colloids*, **2001**, *801*, 23-39.
- [12] Kim, A. Y.; Berg, J. C. *Langmuir*, **2000**, *16*, 2101–2104.
- [13] Cölfen, H.; Mann, S. *Angew. Chem. Int. Edit.*, **2003**, *42*, 2350-2365.

- [14] Keledi, G.; Hári, J.; Pukánszky, B. *Nanoscale*, **2012**, *4*, 1919-1938.
- [15] Majumdar, A.; Kim, J.; Vuckovic, J.; Wang, F. *Nano Lett.*, **2013**, *13*, 515-518.
- [16] Huang, X.; Zeng, Z.; Fan, Z.; Liu, J.; Zhang, H *Adv. Mater.*, **2012**, *24*, 5979-6004.
- [17] Venugopal, A.; Colombo, L.; Vogel, E. M. Contact resistance in few and multilayer graphene devices. *Appl. Phys. Letter*, **2010**, *96*.
- [18] Xiao, L.; Chen, Z.; Feng, C.; Liu, L.; Bai, Z. Q.; Wang, Y.; Qian, L.; Zhang, Y.; Li, Q.; Jiang, K.; Fan, S. *Nano Lett.*, **2008**, *8*, 4539-4545.
- [19] Shin, K, Y.; Hong, J, Y.; Jang, J. *Chem. Commun.*, **2011**, *47*, 8527-8529.

[20] You, S. A.; Kwon, O. S.; Jang, J. *J. Mater. Chem.* **2012**, *22*, 17805-17812.

[21] Shin, K.Y.; Hong, J.Y.; Lee, S.; Jang, J. *J. Mater. Chem.* **2012**, *22*, 23404-23410.

[22] Chanmal, C. V.; Jog, J. P. *Int. J. Plast. Technol.*, **2011**, *15*.

[23] Khudiyev, T.; Ozgur, E.; Yaman, M.; Bayindir, M. *Nano Lett.*, **2011**, *11*, 4661-4665.

[24] Stöber, W.; Fink, A. *J. Colloid Interf. Sci.* **1968**, *26*, 62-69.

[25] Dang, Z. M.; Wang, H. Y.; Xu, H. P. *Appl. Phys. Letter*, **2006**, *89*.

[26] Martins, P.; Caparros, C.; Gonçalves, R.; Martins, P. M.; Benelmekki, M.; Botelho, G.; Lanceros-Mendez, S. *J. Phys. Chem. C*, **2012**, *116*, 15790-15794.

[27] Mohajir, B. E. E.; Heymans, N. *Polymer*, **2001**, *42*, 5661-5667.

- [28] Mendes, S. F.; Costa, C. M.; Caparros, C.; Sencadas, V.; Mendez-Lanceros, S. *J. Mater. Sci.* **2012**, *47*, 1378-1388.
- [29] Lee, S.; Hong, J. Y.; Jang, J. *Poly. Int.*, **2013**, *62*, 901-908.
- [30] Cheng, J.; Zhang, J.; Wang, X. *J. Appl. Polym. Sci.*, **2013**, *127*, 3997-4005.
- [31] Kim, G. H.; Hong, S. M.; Seo, Y. *Phys. Chem. Chem. Phys.*, **2009**, *11*, 10506-10512
- [32] Hong, J.Y.; Lee, E.; Jang, J. *J. Mater. Chem. A*, **2013**, *1*, 117-121.
- [33] Van Beek, L. K. H.. *Physica* **1960**, *26*, 66-68.
- [34] Bhimasankaram, T.; Prasad, G. *Curr. Sci.* **1998**, *74*, 967-976.

초 록

저음역대가 향상된 불소수지 압전 필름 스피커를 제조 하였다. 고농도의 바륨이 도핑된 이산화규소와 이산화티타늄으로 이루어진 나노 필러 제조하여 전기방사 방법을 이용해 대면적의 불소수지 나노 파이버를 제조 후 압전성을 향상된 필름으로 형태를 변화 시켰다. 이로인해 불소수지의 유전율 및 베타 결정의 함량을 증가 시켰다. 이렇게 제조된 필름에 화학기상증착 방법으로 만들어진 그래핀을 전극으로 사용하여 불소수지 박막 스피커를 최종적으로 개발 하였다. 스피커 성능을 향상 시키기 위한 변수로는 필름 두께와 전극의 종류 그리고 나노 필러의 함량을 조절 하였다. 그 결과 필름의 두께는 80 μm 를 사용하고 전극으로서는 전도도가 가장 향상된 전극을 사용함으로 주파수 응답 특성의 중음역과 고음역대가 향상 되었다. 또한 필러는 불소수지에 15 wt%가 함유 되었을 때 베타 결정이 가장 많이 생성 되었고 이로 인해 저음부가 기존 상용화 불소수지 박막 스피커에 비해 60 % 이상 향상 되었다.

주요어: 박막형 음향 작동기, 불소수지, 화학기상증착 그래핀,

할로우 나노 필터, 결정성

학번: 2011-24099

주요어: 아쿠아스틱 액츄에이터, 화학기상증착 제조 그래핀, 할로우

나노 필터, 결정성.

학번: 2011-24099